

Title	Carbon nanocage supported synthesis of V2O5 nanorods and V2O5/TiO2 nanocomposites for Li-ion batteries
Authors	Armstrong, Mark J.;Burke, David M.;Gabriel, Timothy;O'Regan, Colm;O'Dwyer, Colm;Petkov, Nikolay;Holmes, Justin D.
Publication date	2013-09
Original Citation	ARMSTRONG, M. J., BURKE, D. M., GABRIEL, T., O'REGAN, C., O'DWYER, C., PETKOV, N. & HOLMES, J. D. 2013. Carbon nanocage supported synthesis of V2O5 nanorods and V2O5/TiO2 nanocomposites for Li-ion batteries. Journal of Materials Chemistry A, 1, 12568-12578. doi: 10.1039/c3ta12652h
Type of publication	Article (peer-reviewed)
Link to publisher's version	http://pubs.rsc.org/en/Content/ArticleLanding/2013/TA/c3ta12652h#!divAbstract - 10.1039/c3ta12652h
Download date	2024-05-02 02:44:57
Item downloaded from	https://hdl.handle.net/10468/1352

Cite this: DOI: 10.1039/c0xx00000x

PAPER

www.rsc.org/xxxxxx

Carbon Nanocage Supported Synthesis of V_2O_5 Nanorods and V_2O_5/TiO_2 Nanocomposites for Li-ion Batteries

Mark J. Armstrong,^{a,c} David M. Burke,^{a,c} Timothy Gabriel,^{a,c} Colm O'Regan,^{a,c} Colm O'Dwyer,^b Nikolay Petkov^{a,c} and Justin D. Holmes^{a,c,*}

Received (in XXX, XXX) Xth XXXXXXXXX 20XX, Accepted Xth XXXXXXXXX 20XX

DOI: 10.1039/b000000x

Abstract: We present the facile synthesis of crystalline V_2O_5 nanorods and V_2O_5/TiO_2 nanocomposites structures by a carbon nanocage (CNC)-assisted growth process, using vanadium triisopropoxide oxide and titanium isopropoxide precursors in air at 500 °C. The diameters of the resultant V_2O_5 nanorods ranged between ~ 10 – 70 nm, while the crystalline V_2O_5/TiO_2 nanocomposite structures adopted a unique morphology, due to both crystallisation and templating processes, with V_2O_5 adopting small-diameter nanowire and nanorod morphologies surrounded by sub-30 nm TiO_2 nanoparticles. The V_2O_5 nanorods and V_2O_5/TiO_2 nanocomposites were characterised by electron microscopy and X-ray diffraction techniques and subsequently reviewed as positive Li-ion electrodes. The phase-pure V_2O_5 nanorod structures exhibited appreciable Li^+ storage properties over the potential range of 2.0 – 4.0 V vs. Li/Li^+ , displaying capacities of up to 288 mA h g⁻¹ with appreciable cyclic behaviour at test rates of up to ~ 1 C. The crystalline V_2O_5/TiO_2 nanocomposite structures displayed similar Li^+ storage properties, however, increasing molar fractions of TiO_2 led to a decline in the overall capacity versus the single-phase V_2O_5 counterparts. Interestingly, the Li^+ insertion behaviour of the V_2O_5/TiO_2 nanocomposite displayed character more-typical of amorphous V_2O_5 , which was ascribed to a structural buffering effect of the inactive TiO_2 phase.

Introduction

The ever-increasing popularity of modern portable electronic devices, electric vehicles (EVs)/hybrid electric vehicles (HEVs) etc., has necessitated the research and development of rechargeable batteries with the requisites to meet rising demand. To this end, much effort has been focused on the discovery and development of novel electrode materials with increased capacity, cell voltage, cycling ability and enhanced rate performance.^{1–4} One such candidate, is layered vanadium oxide, V_2O_5 .^{5,6} Vanadium is known to exhibit a wealth of compounds over its range of oxidation states (+2 ... +5), while access to its multiple redox couples at relatively high potentials allows for theoretical capacities up to ~ 440 mA h g⁻¹. As a consequence of intercalation, the characteristically layered orthorhombic V_2O_5 undergoes a series of structural modifications based on a puckering or gliding of the layers, to form a series of related phase $Li_xV_2O_5$.^{7–9} Once transformed, reversible intercalation proceeds in an irreversible γ - V_2O_5 phase, and is entertained over the region of $0.0 \leq x \leq 2.0$, leading to theoretical capacities of V_2O_5 approaching 295 mA h g⁻¹.^{10,5,11,12} Although a third Li^+ insertion is possible ($2.0 \leq x \leq 3.0$), its arrival effects an irreversible structural change to a cubic ω - V_2O_5 phase, having a

typical rock-salt structure. Whilst the rock-salt structure minimises internal electrostatic interactions,⁸ electrochemical cycling of the ω -phase is often only considered for values of x between $0.4 \leq x \leq 3.0$ as a result of its unfavourable crystal orientation.¹³

Although the capacity of V_2O_5 cathodes are known to approach theoretical limits during early stages of cycling, capacity fading as a result of continued Li^+ trapping is known to be problematic. To alleviate this concern, various approaches have been adopted to improve the cyclic stability of V_2O_5 . For example, by restricting lower cut-off potentials to 2.5 V (where $x \leq 1.0$), cycling ensues involving only modest structural changes and a return to the pristine orthorhombic phase is possible after charging. Such cells however, are restricted to lower capacities (~ 147 mA h g⁻¹), and thus present largely insignificant advantages compared to other conventional cathodes. Other possibilities which have been explored include the introduction of guest species such as Ag and Cu, which significantly enhance the electrical conductivity through V_2O_5 ,^{14,15} increasing the interlayer separation distance, or the adoption of composite electrode mixes. Carbon compositing for example, results in increased electrical conductivity while presenting a buffering matrix which may accommodate some of the strain associated

with volume changes induced by electrochemical cycling. As a result, $\text{V}_2\text{O}_5/\text{C}$ composite electrodes have displayed enhanced Li-ion performance, with increased rate capability with high cyclic stability.^{16–18} $\text{V}_2\text{O}_5/\text{TiO}_2$ composite structures have long been known for their synergistic catalytic activity,¹⁹ while Minnett and Owen²⁰ first demonstrated their unique relationship when paired as a potential Li-ion cathode. Subsequent reports have since demonstrated an agreeable cyclic improvement in $\text{V}_2\text{O}_5/\text{TiO}_2$ architectures, however, there still remains variable opinion on the effect of overall capacity.^{21,22,20,23–26} For example, Minnett and Owen²⁰ reported a reduction in discharge capacity for their mixed $\text{V}_2\text{O}_5/\text{TiO}_2$ cathodes on increasing the TiO_2 content, while Davies et al.,²⁵ reported that low wt. % TiO_2 inclusions favoured an increase in the discharge capacity. A more recent report by Sahana et al.,²² found variability among the discharge capacities of $\text{V}_2\text{O}_5/\text{TiO}_2$ systems which was ascribed to variances in the synthetic procedure. These findings have been established among both crystalline and also amorphous $\text{V}_2\text{O}_5/\text{TiO}_2$ systems including physical mixtures.

A number of synthetic approaches have been utilised in the preparation of nanostructured V_2O_5 including sol-gel,^{27–29} hydro/solvothermal,^{30–32} reverse-micelle,^{33,34} polyol,³⁵ electrospinning,^{36–40} and hard/soft templating.^{41–46} Typically, $\text{V}_2\text{O}_5/\text{TiO}_2$ composites have been prepared for electrochemical use as either amorphous or crystalline thin-films by conventional sol-gel chemistries using the respective metal alkoxide precursors.^{21,22,20,23–26} Templated synthesis of nanomaterials is a particularly useful approach combining solution or gas phase chemistries with either hard-templates, *e.g.*, anodic alumina oxide (AAO) membranes, mesoporous carbon/ SiO_2 etc. or soft-templates, *e.g.*, micellar solutions or liquid crystals. The use of mesoporous SiO_2 or carbons acting as hard-templates has been widely demonstrated in the literature, where the loading and subsequent removal of such templates has resulted in the creation of a number of nanostructured or inverse replica materials.^{47,48} In this paper, we highlight the remarkably facile synthesis of V_2O_5 nanorods and $\text{V}_2\text{O}_5/\text{TiO}_2$ nanocomposite structures obtained using carbon nanocages (CNCs) acting as a hard support templates. The CNCs were subsequently removed following thermal treatment in air at 500 °C which also facilitated the crystallisation of the active materials. The V_2O_5 nanorods and $\text{V}_2\text{O}_5/\text{TiO}_2$ nanocomposite materials produced were characterised by X-ray diffraction (XRD), scanning electron microscopy (SEM), transmission electron microscopy (TEM) techniques and reviewed as potential Li-ion positive electrode materials by means of chronopotentiometric measurements. The single-phase V_2O_5 nanorod structures exhibited appreciable Li^+ storage properties over the potential range of 2.0 – 4.0 V vs. Li/Li^+ , displaying capacities of up to 288 mA h g^{-1} at a specific current of 50 mA g^{-1} . The crystalline $\text{V}_2\text{O}_5/\text{TiO}_2$ nanocomposite structures displayed similarly appreciable Li^+ storage properties over the same potential region, however, increasing molar fractions of TiO_2 led to a greater decline in the overall capacity versus the single-phase V_2O_5 counterparts as a consequence of increasing inactive (TiO_2) content.

Experimental Section

Carbon nanocage (CNC) templates were synthesised using a

supercritical fluid (SCF) deposition method previously reported by Li et al.⁴⁹ Typically, 0.5 g of Co/Mo/MgO catalyst was placed in a reaction cell which was heated to 700 °C at a rate of 5 °C min^{-1} under a flow of argon (200 ml min^{-1}). The catalyst was reduced in 10 % H_2/Ar for 30 min at a flow rate of 200 ml min^{-1} . 3 ml of *p*-xylene was placed in the front part of a delivery cell, separated by a piston, in a water bath at 40 °C. The front part of the cell was then charged with CO_2 up to the desired reaction pressure of 10.34 MPa using an ISCO pump. The contents of the SCF cell were flowed over the catalyst material in the reaction cell and CO_2 was applied to the back of the piston in the delivery cell to maintain a constant pressure throughout the course of the reaction. After the reaction was complete, the cell was depressurised and allowed to cool to room temperature under a flow of argon (200 ml min^{-1}). The catalyst material was removed by stirring in 3 M HNO_3 for 4 h, then filtered and washed with deionised water until the acidity of the filtrate was at pH 6, and finally dried at 60 °C in an oven for 24 h.

For the synthesis of the V_2O_5 nanorods, the CNCs were weighed into a sample vial and transferred to a glovebox (Innovative Technology corp.), where O_2 and H_2O levels were below 0.1 ppm. The liquid precursor, vanadium(V) triisopropoxide oxide (VTIPO) (99.9 %, ABCR), was then slowly introduced into the vial via a micropipette. The amount of liquid precursor used was determined from the pore volume of the CNCs (typically $\sim 3 - 5 \text{ cm}^3 \text{ g}^{-1}$). Once removed from the glovebox, the vial was slowly introduced to ambient conditions by piercing the vial cap several times where the precursor was then allowed to hydrolyse under ambient conditions overnight. The CNC/VTIPO composites were then subjected to thermal treatment in an open tube furnace at a temperature of 500 °C for 4 h under a heating rate of 1 °C min^{-1} , forming the final yellow/orange V_2O_5 powder product. For the preparation of the $\text{V}_2\text{O}_5/\text{TiO}_2$ nanocomposites, the CNCs were treated in the same manner described above except mixtures of vanadium triisopropoxide oxide and titanium(IV) isopropoxide were first prepared according to V:Ti molar ratios of 100:0, 90:10, 75:25 and 70:30, respectively. For comparative purposes, TiO_2 powders were also prepared by the sole addition of titanium(IV) isopropoxide to CNCs and treated in the same manner. X-ray diffraction (XRD) measurements were performed on a Phillip's XPERT MPD Pro diffractometer using Cu K α radiation (1.5406 nm) operating at 40 kV and 35 mA. Scanning electron microscopy (SEM) images were collected on a FEI Quanta 650 microscope operating at 10 kV and transmission electron microscopy (TEM) images were collected on a JEOL JEM 2100 TEM operating at 200 kV. EDX spectra were collected on an Oxford Instruments (INCA) EDX system fitted to the TEM. Thermogravimetric analysis (TGA) was carried out at a heating rate of 40 °C min^{-1} in air using a Mettler Toledo TGA/DSC1 STAR system, while N_2 sorption measurements of the CNC and TiO_2 powder samples were performed on a Micromeritics Tristar II 3020 BET Surface area analyser.

For the electrochemical measurements, electrode slurries were prepared by thoroughly mixing and grinding the active powder, acetylene black (Alfa Aesar, corp.), and PVDF (Sigma-Aldrich) in a ratio of 75:20:5 by mass, respectively. Absolute EtOH was used to ensure adequate consistency of the slurries. The slurries

were then cast on to pre-cleaned Al-foil and dried at 120 °C for several hours before mechanically pressing and further drying at 120 °C for at least 24 h. CR2025-type coin cells were assembled in a glovebox filled with high purity Ar gas, using pure Li chips (MTI corp.), serving as the negative electrode and Celgard® 2320 PE/PP/PE membranes as separator. The electrolyte was a solution of 1M LiPF₆ in EC:DMC (50:50 v/v). Galvanostatic cycling was carried out in the potential range between 2.0 – 4.0 V vs. Li/Li⁺ using a Princeton Applied Research (V3) potentiogalvanostat. Current densities and capacities were determined on the mass of active material loading (including TiO₂).

Results and Discussion

Synthesis and Structural Characterisation of V₂O₅ Nanorods

Crystalline V₂O₅ nanorods were prepared by the ambient and temperature-driven hydrolysis of the liquid precursor vanadium triisopropoxide oxide (VTIPO), using carbon nanocages (CNCs) as support templates. CNCs are an example of high surface area nanoporous carbon materials with a hollow cage-like structure. Their formation has been previously expressed in low yields as a by-product of CNT growth, although various synthetic methods are now utilised to produce CNCs as the major product. Li *et al.*⁴⁹ identified a SCF growth process which could produce small diameter (20 – 60 nm) CNCs with remarkably high mesopore volumes (up to 5.8 cm³ g⁻¹), and surface areas exceeding 1200 m² g⁻¹, formed as the major product of a decomposition reaction of carbonaceous precursors (*p*-xylene) over cobalt-molybdenum particulate templates supported on MgO. Highly porous CNCs, whose cage-like exterior consists of multiple (5 – 10) layers of pseudo-graphitic shells, followed as a result of annealing at high-temperature and subsequent removal of the metal catalyst templates by acid washing. Although such methods have produced CNCs in high yield, their existence is not typically monodisperse and their morphologies are varied, owing to the wide size and shape distribution of the Co/Mo template. Congruently, the CNCs produced in this fashion do not generally exceed 60 nm in length and coupled with their extraordinarily high mesopore volume and surface area, makes them suitable support templates for the adsorption of metal species,⁵⁰ or alternatively, in the preparation of other nanostructures. While examples of using carbon, *e.g.*, multi-walled carbon nanotubes (MWCNTs), as support templates in the preparation of nanostructured metal oxides such as V₂O₅ exist,^{51,52} to our knowledge no such example has been demonstrated using CNCs in this manner.

VTIPO was chosen as the vanadium oxide precursor given its liquid nature at room temperature, while affording a direct route to V₂O₅ following complete hydrolysis; 2VO(OR)₃ + 3H₂O → V₂O₅ + 6ROH (R = C₃H₇).²⁷ Hydrolysis of VTIPO may be initiated at room temperature under ambient moisture however, the rate of hydrolysis is often controlled in a more exacting fashion by adopting various solvent (typically, IPA:H₂O), ratios under strict conditions. In our study, VTIPO was added to the CNC templates without pre-dilution (typically in measures of μL), under inert conditions in a sample vial before exposing to ambient conditions for several hours. In a parallel test, exposure

of VTIPO to ambient moisture in the absence of CNC template resulted in a largely uncontrollable deposition of orange/yellow species (presumably amorphous V_xO_y), onto the sides of the glass vial driven by the high vapour pressure of 2-propanol formed during hydrolysis. Conversely, no such deposition was evidenced with the CNC-templated samples, indicating that VTIPO had successfully adsorbed onto the surfaces of the CNCs or had been effectively driven inside the mesopore volume by capillary forces. The CNC template therefore accommodated the partial hydrolysis of VTIPO in a controllable manner.

Thermogravimetric Analysis (TGA) of a typical VTIPO/CNC sample collected after approximately 24 h of ambient exposure (see electronic supplementary info. Figure S1), depicts a loss of approximately 15 wt. % of the VTIPO/CNC sample before reaching a temperature of 150 °C, while the majority of weight loss (~45 wt. %), occurs in the temperature range between 330 – 450 °C, which is ascribed to the removal of the CNC template by combustion. Accordingly, vanadium and other transition metal oxide composites (V₂O₅, TiO₂, WO₃ etc.), are known to catalyse the oxidation of organic compounds⁵³ thus, removal of the CNC template may proceed proficiently under thermal treatment. Plateauing in the TGA profile (> 450 °C), indicated that removal of the CNC template was complete at this stage. During such time, further crystallisation and growth of V₂O₅ and loss of residual carbon from the CNC template is possible. Since crystallisation of V₂O₅ is predicted at temperatures exceeding the onset of CNC combustion (330 – 450 °C), complete removal of the CNC template is both concomitant and necessary in order to achieve adequate crystallisation. A temperature of 500 °C was therefore used to ensure complete carbon removal and maximum crystallisation of V₂O₅. After thermal treatment at 500 °C, a fine yellow/orange powder typical of V₂O₅ was obtained. The formation of crystalline V₂O₅ was confirmed by wide-angle XRD analysis, as displayed in figure 1. All diffraction lines could be indexed to the scheherbinaite (orthorhombic) phase of V₂O₅ (JCPDS card: 41-1426; with lattice parameters *a* = 1.1516, *b* = 0.3536, *c* = 0.4372 nm), while no distinct diffraction lines originating from other VO_x phases were identified in the XRD profile, indicating a phase-pure formation of V₂O₅.

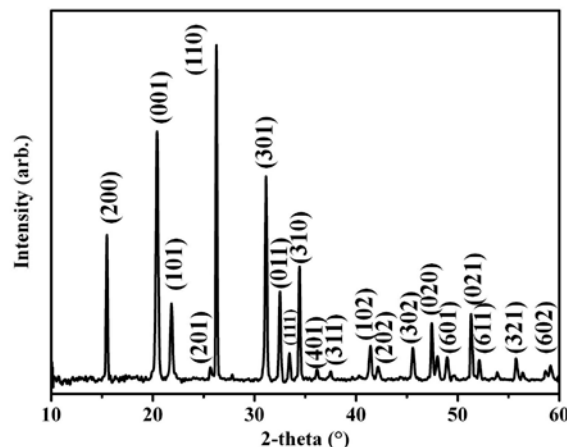


Fig. 1 Background-removed XRD pattern of V₂O₅ nanorods obtained after thermal treatment in air at 500 °C for 4 h. Reflections are indexed to shcherbinaite-phase V₂O₅ (JCPDS card: 41-1426).

Analysis of the morphology and structure of the resultant

V_2O_5 nanorods was conducted by electron microscopy and is shown in figure 2. The SEM image in figure 2(a) shows the aggregation of the CNCs into larger particle clusters while the TEM image of the bare CNC support template, as displayed in figure 3(c), shows the morphological variation of the CNCs owing to the original size and shape distribution of the catalyst particles from which they are formed and outlines the densely packed, hollow, rod-like structuring consisting of concentrically laid pseudo-graphitic carbon layers. The degree of graphitisation is dependent on the annealing temperature used during CNC synthesis, which in our case was carried out between 700 – 750 °C.⁴⁹ After inclusion of the VTIPO precursor and the subsequent thermal treatment at 500 °C, the V_2O_5 nanorods (figure 3(b) to (d)), can be seen to adopt a similar clustering to that of the CNC support template. SEM analysis revealed the V_2O_5 nanorods ranged between 20 – 100 nm in diameter with lengths of up to 300 nm. The effect of annealing time was also investigated by varying the thermal treatment between 30 – 240 min, but no apparent change in morphology or size distribution of the V_2O_5 nanostructures was observed. Samples prepared in the absence of the CNC support templates, using the same liquid VTIPO precursor, also displayed similar morphologies; however, a range of larger, plate-like particles and an apparent greater size distribution was evident (figure 2(e)). In addition, the preparation of these template-free samples was cumbersome and often resulted in poor yield. The formation of rod or elongated V_2O_5 structures is not uncommon and has been observed as a result of many synthetic routes, as a consequence of the high degree of anisotropic bonding.

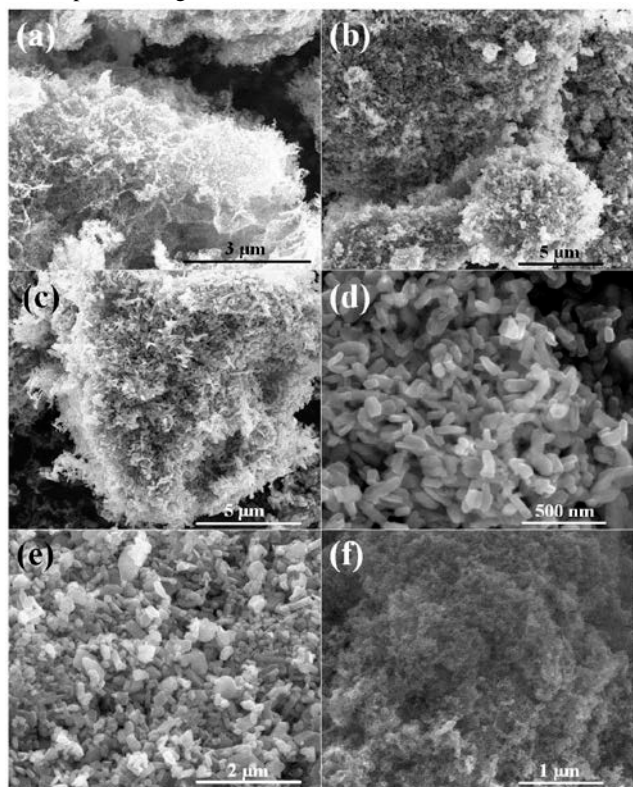


Fig. 2 SEM images of (a) a CNC template loaded with the VTIPO precursor before pyrolysis, (b – d) V_2O_5 nanorods obtained after removal of the CNC template and annealed at 500 °C in air, (e) V_2O_5 nanorods prepared in the absence of a CNC template and (f) mesoporous TiO_2

nanoparticles obtained using the same procedure with titanium(IV) isopropoxide only.

TEM images of the V_2O_5 nanorods are displayed in figures 3(a) and (b). Exposure time to the electron beam was restricted as V_2O_5 is known to undergo a rapid structural (orthorhombic to cubic) rearrangement under high voltage Joule heating from the electron beam.⁵⁴ The clearly observable lattice fringes which extended along the lengths of the nanorods indicated their highly crystalline nature. A d-spacing of 5.7 Å (the largest among orthorhombic- V_2O_5) relating to the (200) set of crystal planes was discernible, indicating that the V_2O_5 nanorods had a preferred growth in the [010] direction, which is the fastest growth direction in V_2O_5 . Such findings are generally predicted for bulk V_2O_5 structures since the consecutive VO_5 units, which constitute each of its individual layers, are positioned along the b-axis.^{55,56,10}

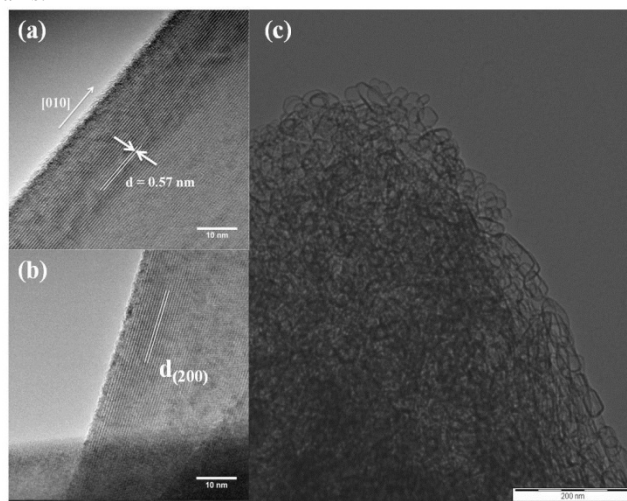


Fig. 3 TEM images of (a, b) V_2O_5 nanorods obtained after thermal treatment at 500 °C for 4 h (scale bar: 10 nm) and (c) CNCs before loading with VTIPO (scale bar: 200 nm).

Previously, MWCNTs have been used as a support template in the preparation of V_2O_5 nanostructures by coating and infilling of their internal cavities by capillary action.^{51,52} Two possible growth environments which occur as a result of our CNC templating process are suggested here. The first suggested mechanism depicted in figure 4(a), is that VTIPO enters the interior volume of the CNCs by capillary force, where subsequently the liquid precursor may partially hydrolyse resulting in amorphous V_2O_5 formation within CNC interior. Elongation or growth of the V_2O_5 particles may then be suitably arrested by the CNC exterior during early thermal treatment. Further crystallisation is then possible until such temperatures where the CNC templates are removed by combustion (> 330 °C). Further elongation or growth of the V_2O_5 nanorods may then ensue as a result of increasing crystallisation energy as a result of the CNC template removal procedure. [Note: V_2O_5 crystallisation (ageing) is known to occur in ambient conditions for up to 1.5 years before stabilising]. While limited, this mechanism would explain the small size increase of the V_2O_5 nanorods versus that of the CNC template. A second plausible mechanism for the formation of V_2O_5 nanorod structures is ascribed to the uptake of VTIPO within the larger mesopore

volume. The mesopore volume originates from two distinct regions; (1) the interior of the CNC, which is relatively small, and (2) the interstitial space formed as a result of agglomeration which accounts for the high surface area. The contribution of both regions to the mesopore volume has been previously identified by their bi-modal pore distribution collected from N_2 -sorption measurements.⁴⁹ The second mechanism may account for the formation of V_2O_5 nanorods in similar fashion, whereby the exterior of the CNCs provide not only numerous nucleation sites, but also act as a steric barrier for growth given their dense packing nature. In support of both proposed mechanisms, figure 4(d) and (e) shows TEM images of a CNC/VTIPO sample collected after ambient exposure followed by thermal treatment at 300 °C in air for 4 h. Under such conditions, partial crystallisation of V_2O_5 is possible whilst maintaining the structural integrity of the CNC template. The TEM images clearly display both filled (having crystalline cores) and empty CNCs, indicating that uptake of liquid VTIPO precursor was possible through the CNC interior volume, while the visibly darker regions indicate a decrease in contrast due to possible instances of amorphous V_xO_y on the exterior CNC surface and within interstitial regions. EDX analysis, shown in figure 4(f), confirms the existence of elemental V and O (intense peaks), while all other species identified (C, Fe, Co, Cu), originate from the Cu-alloy grid and TEM sample holder. No separate or otherwise distinct crystalline morphologies were identifiable by TEM indicating the bulk of small particulate material is likely found within the larger mesopore volume.

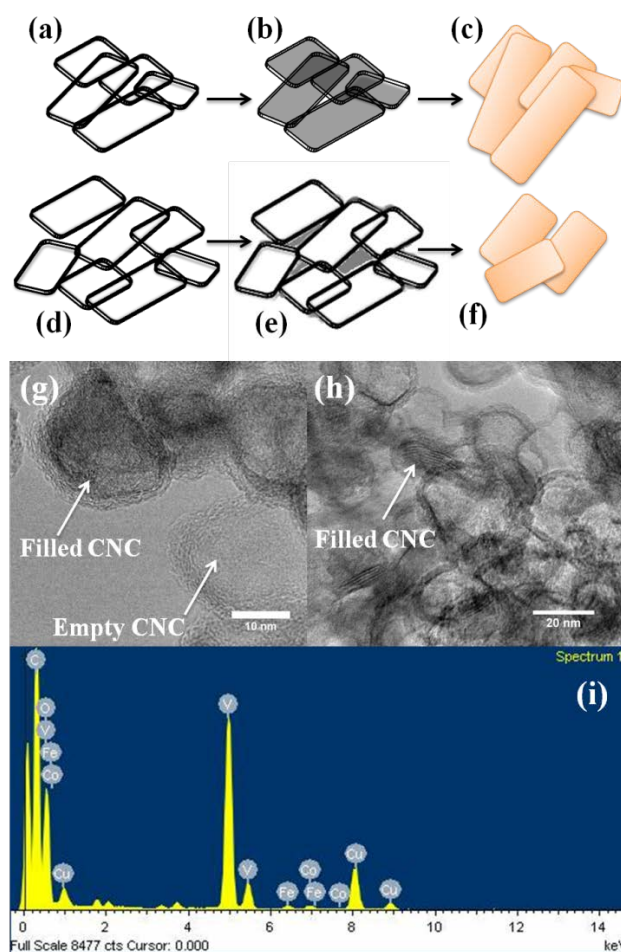


Fig. 4 Schematic of a possible formation route of V_2O_5 nano-rods by a CNC-supported templating process: (a,d) empty CNC template, (b,e) CNC template loaded with liquid precursor (VTIPO) and (c,f) removal of template by pyrolysis yielding V_2O_5 nanorods; (g) and (h) TEM images showing empty and filled CNCs after thermal treatment of VTIPO/CNCs in air at 300 °C and (i) corresponding EDX spectra showing V, O peaks, collected over the area of (h).

Synthesis and Structural Characterisation of V_2O_5/TiO_2 Nanocomposites

V_2O_5/TiO_2 nanocomposites were prepared following a similar CNC-supported procedure by adopting a mixture of VTIPO and the analogous liquid TiO_2 precursor, titanium(IV) isopropoxide. In our study, the V:Ti molar fractions that were used were 90:10, 75:25, 70:30 and 0:100, respectively.

XRD was used to confirm the crystalline identity of the nanocomposite structures and is displayed in figures 5(a) to (c). Subsequent analysis confirmed the existence of separate crystalline phases consisting of orthorhombic V_2O_5 (JCPDS 41-1426), and tetragonal TiO_2 (JCPDS 21-1272). Since it is known that V_2O_5 and TiO_2 do not form solid solutions, the existence of both crystalline V_2O_5 and TiO_2 confirms their composite-structuring. The diffraction patterns originating from V_2O_5 (figure 5, squares), had a similar relative intensity and broadening to those of the V_2O_5 nanorods (figure 1), indicating the presence of small V_2O_5 polycrystallites. The diffraction patterns were notably most intense in the sample of V:Ti ratio 90:10, while the intensity of the V_2O_5 diffraction lines decreased with increasing

TiO₂ content. The reduction in crystallinity of the V₂O₅ component is ascribed to a competing crystallisation mechanism in the mixed-oxide system. The XRD profile displaying broad reflections of small-diameter anatase TiO₂ nanoparticles prepared from titanium isopropoxide (V:Ti 0:100), is shown in figure 5(d). All diffraction features within this phase-pure TiO₂ sample were identifiable in the V₂O₅/TiO₂ composite XRD patterns, indicating the formation of a similar TiO₂ phase. The TiO₂ powder had a measured surface area of ~ 90 m² g⁻¹ (see supporting info. figure S4) due to regions of distinctly porous structuring as a result of inter-particle agglomeration. The relatively high surface area and unique porous structuring of the TiO₂ powder thus illustrated the practicality of CNC templating process in the facile preparation of TiO₂ and potentially, a whole host of other nanostructured materials.

The typical morphology of the V₂O₅/TiO₂ nanocomposites structures is displayed in figure 6. SEM analysis revealed the V₂O₅/TiO₂ nanocomposites exhibited similar clustering to the single-phase V₂O₅ nanorods (figure 7(a)). The morphologies of the individual components, however, consist of small-diameter nanowires and some slightly larger elongated nanorods surrounded by small-diameter nanoparticles. EDX spectroscopy confirmed the elemental identity of the individual nanostructures, confirming the presence of vanadium and oxygen in the nanowire/nanorod structures and titanium and oxygen in the nanoparticles (see electronic supplementary info. fig. S2).

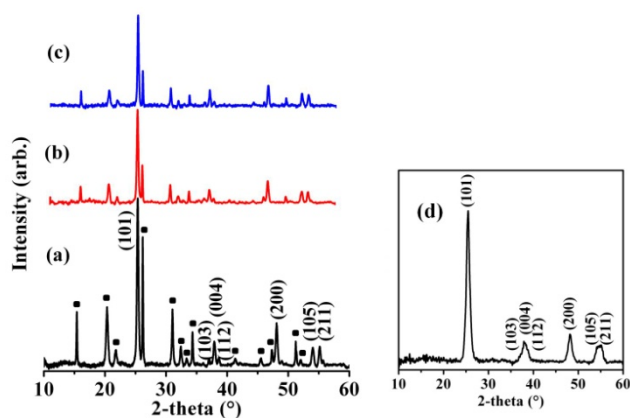


Fig. 5 XRD profiles of V₂O₅/TiO₂ nanocomposites obtained from a V:Ti molar ratio of: (a) 90:10, (b) 75:25 and (c) 70:30. Solid squares indicate

schcherbinaite-phase V₂O₅ (PDF: 41-1426), while the peaks labelled with (hkl) indicate rutile-TiO₂ (PDF 21-1272) and (d) XRD profile of TiO₂ nanoparticles obtained from titanium isopropoxide/CNCs after thermal treatment at 500 °C for 4 h in air.

The V₂O₅ nanowires ranged in diameter from ~ 10 – 50 nm having lengths of up to ~ 1.5 μm, which represent some of the smallest diameter V₂O₅ structures reported in the literature. Conversely, the larger V₂O₅ nanorods ranged in diameter between ~ 30 – 150 nm while no appreciable difference in morphology was discernible amongst samples of different constituent V:Ti molar fractions. Compared to phase-pure V₂O₅ nanorods prepared in the absence of TiO₂, which displayed lengths up to ~ 150 nm, the V₂O₅ nanocomposite structures possessed considerably higher aspect ratio, regardless of their rod or wire morphology. The elongation of the V₂O₅ phase in this case is made possible by the influence of the titania precursor during crystallisation. Such influences have been reported in previous studies where additions of titania precursor sols have resulted in a reduction of the V₂O₅ grain size.^{21,20} Similarly, the addition of low wt. % vanadia sols can result in the reduction of the mean diameter of TiO₂ particles and a hindering of the anatase to rutile conversion process with increasing calcination temperature.⁵⁷ These findings have been previously explained by an increased requirement for diffusion during crystallisation in the mixed oxide system.²⁴ In our study, the conditions for the growth of V₂O₅ nanorods and V₂O₅/TiO₂ nanocomposites remained appreciably similar, which is an important point when considering the morphological difference between V₂O₅ in the single phase (short nanorods), to those in the mixed V₂O₅/TiO₂ nanocomposite (elongated nanorods/nanowires). Such morphological differences may be ascribed to the variances in growth environment existing in the mixed-oxide system, where two separate phases (V₂O₅ and TiO₂), must crystallise in parallel; with both growth species in the mixed state, the rate of diffusion of adatoms to the surface facets of the growing crystal could be expected to slow as a result of both an increase in diffusion length and the competition for energy. Such retardation effects may impart severe changes to the crystal habit resulting in concomitant elongation in axial directions leading to anisotropic growth. Such a scenario would, in our case, explain the significant elongation of the orthorhombic V₂O₅ phase and would be associated with a change in the nominal growth direction.

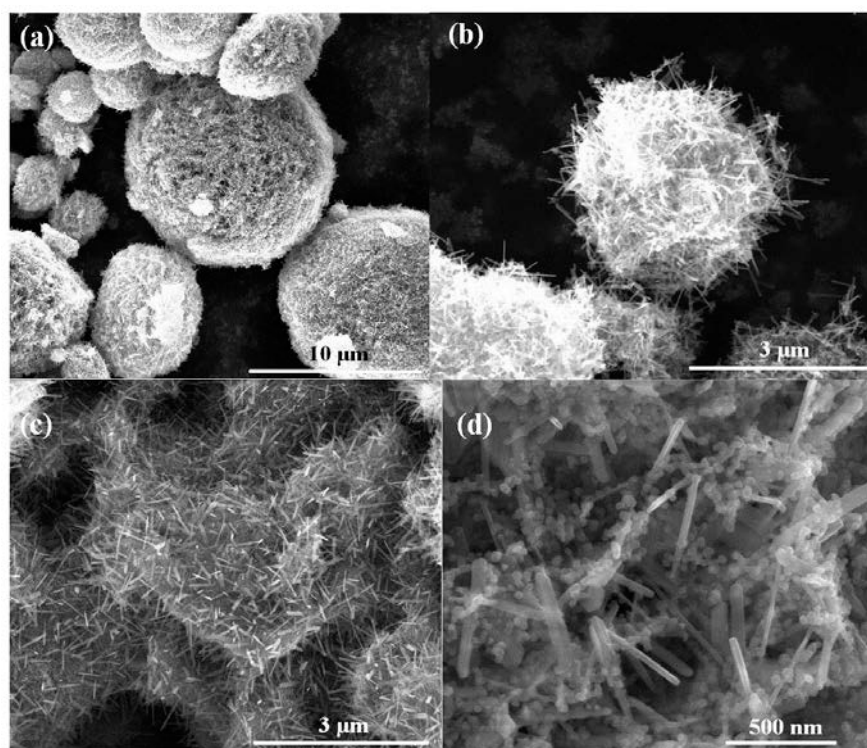


Fig. 6 (a)-(d) SEM images of V_2O_5/TiO_2 nanocomposites prepared from a molar ratio of 90:10 V:Ti after removal of the CNC template at 500 °C.

TEM analysis was employed to confirm the structural nature of nanocomposite structures and is displayed in figure 7. High resolution images of the 1D nanostructures (figures 7(a) to (d)), confirms that no solid solutions formed and that the small-diameter elongated nanorods were quasi single-crystalline in nature. Such findings may be expected for crystalline V_2O_5/TiO_2 nanocomposites, however, amorphous thin-films have been suggested to contain a partial substitution of Ti for V within the V_2O_5 crystal lattice.^{21,58} The clear lattice fringes (figures 8(c) and (d)), represent a d-spacing of 3.4 Å which

corresponds to the interplanar spacing of the (110) set of planes in orthorhombic V_2O_5 (JCPDS: 41-1426). Such findings are in contrast to those of the shorter V_2O_5 nanorods obtained separately, which grew along the faster [010] direction, and confirmed that a different growth mechanism had occurred during crystallisation of the mixed-oxide system. In addition, highly crystalline TiO_2 nanoparticles (figures 7 (e) and (f)), could be identified as existing as a distinctly separate phase. Such findings were determined across all V:Ti molar fractions indicating that the concentration of the respective phases had a limited effect on the morphological outcome of the individual structures.

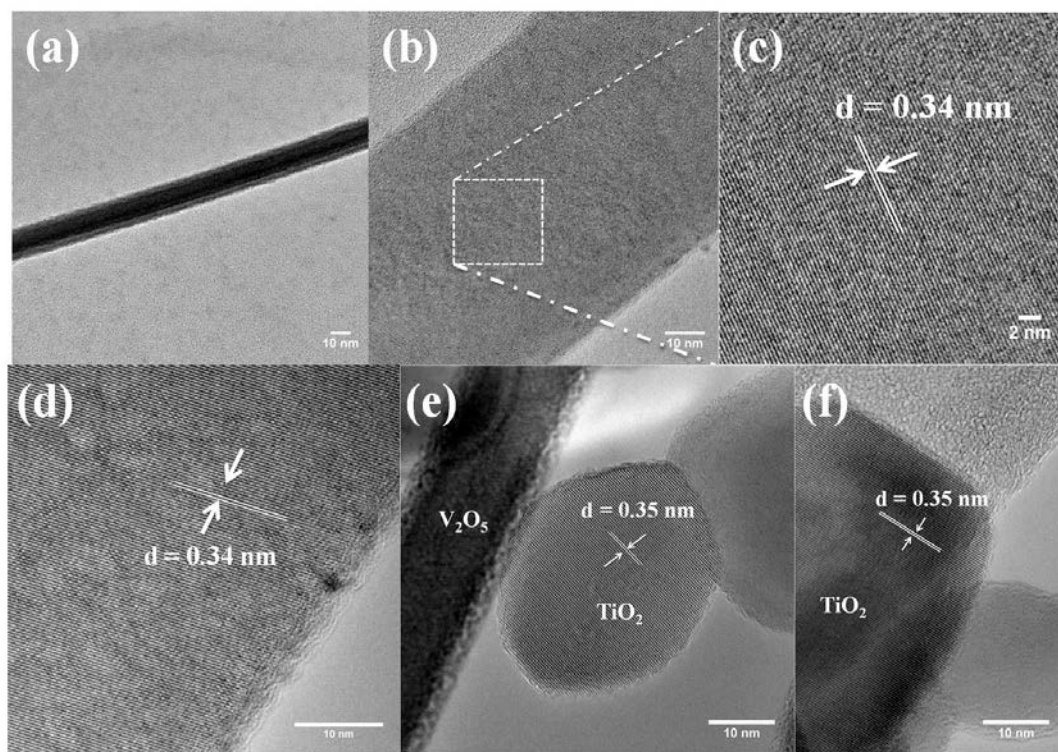


Fig. 7 TEM images of (a) a single V_2O_5 nanowire prepared from a V:Ti molar ratio of 90:10, (b) a larger diameter V_2O_5 nanowire showing associated lattice planes displayed in (c), (d) a V_2O_5 nanorod from prepared from a V:Ti molar ratio of 75:25 and (e) and (f) TiO_2 nanoparticles formed as separate phases adjacent to a V_2O_5 nanowire.

5 Li^+ Storage properties of V_2O_5 Nanorods

A typical first discharge curve taken at a current density of 50 mA g^{-1} ($\sim 0.17 \text{ C rate}$, $1\text{C} = 298 \text{ mA h g}^{-1}$), of the single-phase V_2O_5 nanorods prepared from VTIPO in the presence of CNCs is displayed in figure 8(a). The discharge curve displays a step-wise profile associated with crystalline V_2O_5 , where plateauing regions ensue due to internal structural rearrangements induced as a result of Li^+ insertion.^{7,8,59} Such rearrangements are based on a puckering or gliding of the individual V_2O_5 layers which are stacked along its c-axis; early phase transitions ($\alpha \leftrightarrow \epsilon \leftrightarrow \delta$), are typically accounted for at potentials above 2.5 V and cycling within this cut-off limit typically leads to a return of the pristine orthorhombic phase after charging. In our case, discharging through a $\sim 2.3 \text{ V}$ plateau (where $1.0 < x < 2.0$), resulted in the formation of the irreversible γ - phase, which was retained over subsequent cycles in the region of $2.0 - 4.0 \text{ V vs. Li/Li}^+$. The newly formed γ - phase, which exhibits a more pronounced puckering of the layers compared to that of the δ - phase,^{7,8} facilitates an increase in capacity (of up to 1 Li^+ per V_2O_5 unit), offering reversible Li^+ storage and leading to a final capacity in our first discharge cycle of 288 mA h g^{-1} . This represents approximately 98 % of the theoretical capacity attainable for cycling in the $0.0 < x \leq 2.0$ region. Capacities close to theoretical maxima suggest structural favourability towards Li^+ insertion, which in our case may be ascribed to their small-diameter and hence, short Li^+ diffusion lengths. Typical first discharge cycles of the V_2O_5 nanorods collected over current densities ranging from $50 - 400 \text{ mA g}^{-1}$ ($\sim 0.17 - 1.36 \text{ C rate}$), are displayed in figure 8(b). First discharge capacities of 235, 175 and 152 mA h g^{-1} were attained at the specific currents of 200, 300 and 400 mA g^{-1} ($\sim 0.68, 1.02, 1.36 \text{ C}$, corresponding to 80, 60 and 52% of theoretical capacity, respectively).

Although the discharge capacity decreased notably with increasing current rate, V_2O_5 nanorod morphologies have previously shown considerable promise as high-rate cathodes in lithium cells, with capacities of up to 198 mA h g^{-1} reported at a 4 C rate (1192 mA g^{-1}).⁶⁰ Figure 9(a) displays typical voltage profiles of the V_2O_5 nanorods at a current density of 300 mA g^{-1} ($\sim 1.02 \text{ C rate}$) where the first charge and discharge capacities were 183 and 175 mA h g^{-1} respectively, representing a first cycle Coulombic efficiency ($Q_{\text{discharge}}/Q_{\text{charge}}$) of $\sim 96\%$. The slight overcharge with respect to the initial discharge capacity likely arose due to instances of electrolyte oxidation/formation of the solid electrolyte interphase layer. Galvanostatic cycling of the V_2O_5 nanorods at the current densities of 200 and 300 mA g^{-1} are shown in figure 10(b) where the first charge and discharge capacities at 200 mA g^{-1} were 230 and 225 mA h g^{-1} , respectively, which declined gradually over the first 12 - 15 cycles before showing significantly more stable character in the subsequent cycles. The final discharge capacity attained was 168 mA h g^{-1} , representing a $\sim 75\%$ capacity retention. After the 15th cycle, however, the capacity retention between successive cycle numbers increased to an average $\sim 99.1\%$, indicating further stability in the cyclic behaviour. At the higher current density of 300 mA g^{-1} ($\sim 1.02 \text{ C rate}$), the 1st and 25th discharge capacities were 175 and 139 mA h g^{-1} , respectively, representing an overall capacity retention of $\sim 79\%$ and an average loss between successive cycles of $\sim 1.4\%$. Early capacity fading was less pronounced than at the slower 0.68 C rate , which was likely a consequence of induced polarization, while the lower overall insertion capacity may have led to fewer instances of Li^+ trapping. Overall, the appreciable Li^+ storage

properties of the V_2O_5 nanorod structures may be attributed to their small diameter, dense packing nature (enabling good inter-particle connect), and through their relatively small lengths which could limit the relative size of the (001) facet, unfavourable to Li^+ insertion. The performance thus displayed may therefore serve as a basis for comparison of the effect of TiO_2 inclusion on the Li^+ storage properties of the nanocomposite V_2O_5/TiO_2 structures prepared by a similar CNC templating process.

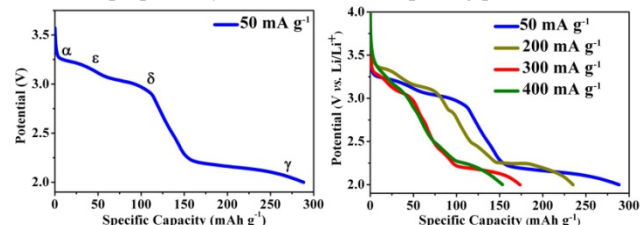


Fig. 8 (a) First discharge curve of V_2O_5 nanorods at a current density of 50 mA g^{-1} ($\sim 0.17 \text{ C}$) between $4.0 - 2.0 \text{ V vs. Li/Li}^+$ and (b) typical first discharge curves of the V_2O_5 nanorods at various current densities between $50 - 400 \text{ mA g}^{-1}$ ($\sim 0.17 - 1.36 \text{ C}$).

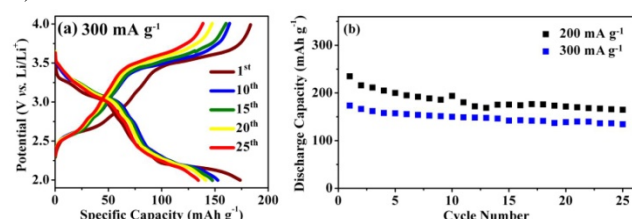


Fig. 9 (a) Charge-discharge curves of V_2O_5 nanorods at a current density of 300 mA g^{-1} ($\sim 1.02 \text{ C}$) between $2.0 - 4.0 \text{ V vs. Li/Li}^+$ and (b) discharge capacity as a function of cycle number at 200 mA g^{-1} ($\sim 0.68 \text{ C}$) and 300 mA g^{-1} ($\sim 1.02 \text{ C}$).

Li^+ Storage properties of V_2O_5 / TiO_2

Typical first charge-discharge plots of the V_2O_5/TiO_2 nanocomposites at a current density of 200 mA g^{-1} ($\sim 0.68 \text{ C}$ rate), are displayed in figure 10(a). The first discharge capacities corresponding to V:Ti molar fractions of 90:10, 75:25 and 70:30 were 223, 217 and 156 mA h g^{-1} , respectively, while the first charge capacities were 231, 198 and 153 mA h g^{-1} , representing Coulombic efficiencies of 100, 91 and 98 %. The shape of the relevant discharge profiles at 200 mA g^{-1} is displayed in figure 10(b), including that of single-phase V_2O_5 , which is shown for comparison purposes. Both V_2O_5 and V:Ti 90:10 samples displayed typically crystalline discharge behaviour having stepwise profiles while interestingly, samples of V:Ti ratios 75:25 and 70:30 displayed monotonic discharge curves more typical of amorphous V_2O_5 behaviour. The amorphous-like behaviour has been noted in previous reports of V_2O_5/TiO_2 composite cathodes, and accompanied by a change in cyclic voltammetric characteristics such as the broadening of oxidation and reduction features.^{21,24,22}

At first hand, such results demonstrate that inclusion of TiO_2 at specific fractions may hinder the respective V_2O_5 phase transitions ($\alpha \leftrightarrow \epsilon \leftrightarrow \delta \rightarrow \gamma$), induced as a result of electrochemical cycling, or alternatively, that the addition of TiO_2 causes significant changes to the degree of crystallisation of the pre-existing V_2O_5 phase. Previously, thin films prepared by Bellenger et al.²³ consisting of amorphous $(V_2O_5)_x-(TiO_2)_{1-x}$

phases have shown that the irreversible γ - V_2O_5 phase does not occur on Li^+ insertion in the $2.0 - 3.0 \text{ V}$ voltage window. Although in our case the constituent phases are crystalline in the first instance, inclusion of greater than 10 mol. % TiO_2 had a pronounced effect on the overall crystallinity of the composite nanostructures. Typically, as a single-phase electrode, anatase- TiO_2 remains for the most part, inactive to Li^+ insertion at potentials above 2.0 V (onset could be expected at or below $\sim 1.8 \text{ V vs. Li/Li}^+$),⁶¹ thus the intercalation ability of TiO_2 remains justifiably limited within our cycling window. Restriction of the lower cut-off potential at 2.0 V may therefore allow a direct analysis of the electrochemical influence of TiO_2 on V_2O_5 phases without enabling a dual intercalative system. Previously, V_2O_5/TiO_2 systems which increased the potential window further to extend below 2.0 V experienced an increase in cell capacity and overall cyclic stability which has been ascribed to the preferential reduction of Ti^{4+} near the low-voltage limit.²⁵ Such an effect has been suggested to restrict the reduction of V^{4+} which may result in higher capacity retention. This explanation, however, does not suffice for cycling within the $2.0 - 4.0 \text{ V}$ region, where TiO_2 remains suitably inactive to Li^+ insertion. To this end, the synergistic effect on the electrochemical performance of the nanocomposite cathodes is considered from the structural viewpoint. An accompanying change in morphology of V_2O_5 as a result of TiO_2 inclusion may account for differences in the overall capacity, stability and rate capability, however, morphological considerations are unlikely to account for the dramatic change in charge-discharge characteristics experienced with increasing TiO_2 fractions. Although high resolution TEM analysis confirmed that the structuring within the composite electrode was crystalline over all V:Ti ratios, XRD analysis (figures 5(a) to (c)), identified a degree of reduced crystallinity amongst the V_2O_5 components with increasing TiO_2 fractions. Such decreases may result in an increasing incidence of amorphous content which may explain the absence of discernible structural changes featured within the voltage profiles. Additionally, it is reasoned that the inclusion of TiO_2 fractions may impart a degree of structural buffering through which a reduction in the extent of atomic scale changes of the V_2O_5 phase is possible. In this case, accommodation of Li^+ at the TiO_2 surface may enable a pronounced stability of the electroactive V_2O_5 surface during discharge, where a degree of inhibition of irreversible phase changes may result. The addition of carbon, for example, is known to significantly reduce the degree of structural degradation as a result of continued volume changes associated with Li^+ intercalation. While solid solutions of V_2O_5 and TiO_2 are unknown, addition of controlled amounts of V_2O_5 to TiO_2 supports have resulted in the growth of an interfacial region existing at the surface of the TiO_2 support.⁶² Such regions are made possible as a result of the small ($\sim 5 \%$), lattice mismatch existing between orthorhombic V_2O_5 and tetragonal TiO_2 .⁶³ In our case, we have also been able to identify a degree surface roughness via HRTEM and a clearly visible stacking boundary existing at some of the V_2O_5 nanowire surfaces (see figure 11). Such interfaces were only identified in the nanocomposite structures indicating their origins arise from TiO_2 . Lattice fringes measuring 0.34 nm , typical of the interplanar spacing of the (110) set of planes in orthorhombic

V_2O_5 , are met by a smaller set of lattice fringes measuring 0.17 nm, which could be ascribed to the (105) set of planes in tetragonal TiO_2 . Evidence of a separate crystalline surface may further support the notion of a structural buffering effect although further work is necessary to elucidate the exact nature of the interfacial regions and their influence on electrochemical activity.

Figure 10(f) shows the comparative plot of discharge capacity versus cycle number for all V_2O_5/TiO_2 composite samples and single-phase V_2O_5 nanorods (shown as comparison), collected at a current density of 200 mA g^{-1} ($\sim 0.68\text{ C rate}$). Since the TiO_2 fraction remains inactive to Li^+ insertion at 2.0 V , the current density and capacity obtained represent that of the active V_2O_5 component only, although the specific capacity obtained was determined from the mass of both components collectively. The cycling profile for all composite ratios followed a similar trend of gradual capacity fading over the first 10 cycles which stabilised somewhat over the subsequent cycling period (25 cycles). At the 25th cycle, the discharge capacities for the V:Ti ratios of 90:10 and 75:25 were ~ 120 and 130 mA h g^{-1} , respectively, while that of 70:30 was $\sim 95\text{ mA h g}^{-1}$. The reduction in discharge capacity as a result of TiO_2 inclusion compared to the single-phase V_2O_5 nanorods ($\sim 165\text{ mA h g}^{-1}$), may be accounted for as a result of an increasing amount of inactive mass within the electrode mix (constituting 10 – 30 mol. % TiO_2). While the V_2O_5 nanorods are expressed for comparative purposes, the unique morphology of the V_2O_5/TiO_2 nanocomposite must also be considered when evaluating the electrochemical performance. Although a decline in the overall capacity was expressed at the relatively high current density of 200 mA g^{-1} , at the lower current density of 50 mA g^{-1} (0.17 C rate), cells of V:Ti ratios 90:10 returned discharge capacities as high as 452 mA h g^{-1} (figure 10(e)), resulting in a large specific energy of $\sim 1089\text{ W h kg}^{-1}$. Lee et al.²¹ and Takahashi et al.²⁴ have also reported an increase in the first discharge capacity of their V_2O_5/TiO_2 thin-film and nanorod-array electrodes, although cyclic performance was not presented. The possible increase in specific capacity in our case may be accounted for by the unique structuring of the active V_2O_5 phase in the composite sample which showed significant elongation, coupled with increasing incidences of amorphous V_2O_5 content. It is well-known that amorphous V_2O_5 has the potential for greater insertion capacities versus its crystalline analogue.⁶⁴ In this instance, the overcapacity likely resulted in significant Li^+ trapping leading to a relatively rapid decline in capacity retention over the subsequent cycles. Such early capacities are, however, significantly higher than those returned for the single-phase V_2O_5 nanorods (288 mA h g^{-1}), over comparable test rates and outline the high-capacity potential of the V_2O_5/TiO_2 architectures at specific ratios.

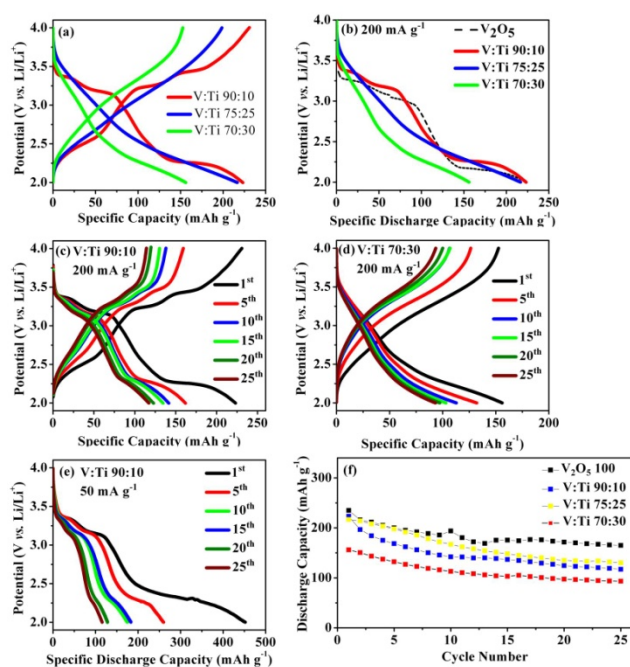


Fig. 10 (a) First charge-discharge curves of V_2O_5/TiO_2 nanocomposites; V:Ti molar ratios of 90:10 (red), 75:25 (blue), 70:30 (green), respectively, collected at a current density of 200 mA g^{-1} (0.68 C rate), between $2.0 - 4.0\text{ V vs. Li/Li}^+$, (b) comparison of the first discharge curves only for single phase V_2O_5 and V:Ti ratios 90:10, 75:25, 70:30 at the same rate, (c) voltage profile of V:Ti 90:10 at a current density of 200 mA g^{-1} , (d) voltage profile of V:Ti 70:30 at a current density of 200 mA g^{-1} , (e) discharge profiles collected from a V:Ti molar ratio of 90:10 at a current density of 50 mA g^{-1} (0.17 C rate) between $2.0 - 4.0\text{ V vs. Li/Li}^+$ and (f) discharge capacity as a function of cycle number (25 cycles) for all V:Ti ratios.

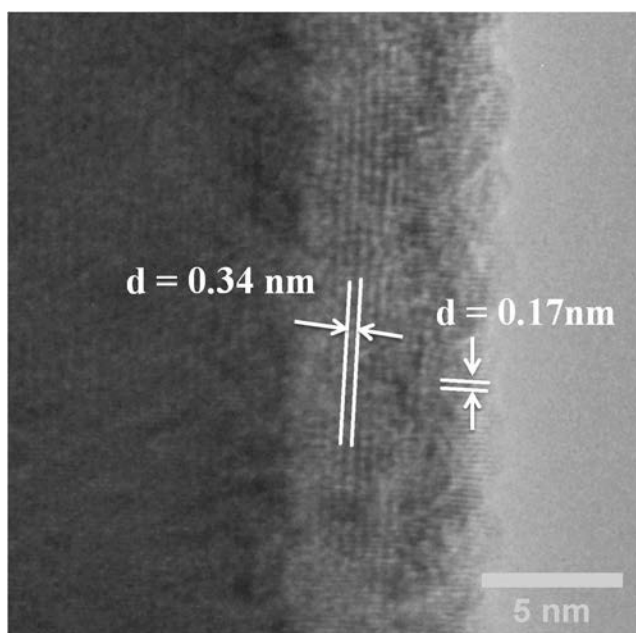


Fig. 11 TEM image of a V:Ti 75:25 nanowire displaying a visible surface interface attributed to a $\sim 5\text{ nm}$ layer of TiO_2 . Visible lattice fringes on the nanowire surface may correspond to the (105) set of planes in anatase TiO_2 (JCPDS: 21-1472).

Conclusions

Small-diameter V_2O_5 nanorods and V_2O_5/TiO_2 nanocomposites with unique morphologies with respect to their single-phase counterparts, were prepared by an extremely facile method utilising the corresponding metal alkoxide precursors loaded on mesoporous carbon nanocage support templates. Template removal and subsequent crystallisation of the individual phases was achieved simultaneously by annealing in air at 500 °C. Addition of 10 – 30 mol. % titanium isopropoxide effected significant changes to the morphology of V_2O_5 due to both templating and slower crystallisation kinetics as a result of dual crystallisation mechanisms. Such changes resulted in the formation of small diameter V_2O_5/TiO_2 nanocomposites under the same processing conditions as those for single-phase V_2O_5 . The single-phase V_2O_5 nanorod structures exhibited appreciable Li-ion performance in the potential range between 2.0 – 4.0 V vs. Li/Li^+ . In contrast, the electrochemical behaviour of the V_2O_5/TiO_2 nanocomposite was significantly altered by increasing amounts of TiO_2 . Cells consisting of > 10 mol. % TiO_2 displayed voltage profiles typical of amorphous V_2O_5 character while evidence of a stacking boundary existing at the V_2O_5 surface could be responsible for restricting large scale atomic changes to the active V_2O_5 material. Future work shall elucidate the exact role of TiO_2 on this electrochemical phenomenon. The facile route and unique morphology of the small-diameter V_2O_5/TiO_2 nanocomposites may also permit their use in other applications such as catalysis, through which the synergistic system may exhibit further interesting behaviour. The CNC-supported synthesis route may also be extended to produce other nanostructured materials such as mesoporous TiO_2 via this facile route.

Acknowledgements

This work was supported by Science Foundation Ireland (SFI) (Grants: 07/SRC/I1172, 08/CE/I1432 and 09/SIRG/I1621). This research was also enabled by the Higher Education Authority Program for Research in Third Level Institutions (2007-2011) via the INSPIRE program. The authors acknowledge the facilities of, and technical assistance from the staff at, Electron Microscopy and Analysis Facility (EMAF) at Tyndall National Institute.

Notes and References

^aMaterials Chemistry & Analysis Group and the ^bApplied Nanoscience Group, Department of Chemistry and the Tyndall National Institute, University College Cork, Cork, Ireland. ^cCentre for Research on Adaptive Nanostructures and Nanodevices (CRANN), Trinity College Dublin, Dublin 2, Ireland

† Electronic Supplementary Information (ESI) available: [TGA data of CNC/VTIPO complex, EDX spectra of V_2O_5/TiO_2 structures and BET plots for CNC templates and porous TiO_2 powders]. See DOI: 10.1039/b000000x/

1. A. Stein, *Nat. Nanotech.*, 2011, **6**, 262–3.
2. J. B. Goodenough and Y. Kim, *Chem. Mater.*, 2010, **22**, 587–603.
3. P. G. Bruce, B. Scrosati, and J.-M. Tarascon, *Angew. Chem. Int. Ed. Engl.*, 2008, **47**, 2930–46.
4. A. Aricò, P. Bruce, B. Scrosati, J. Tarascon, and W. Van, *Nat. Mater.*, 2005, **4**, 366–377.
5. Y. Wang and G. Cao, *Chem. Mater.*, 2006, 2787–2804.
6. Y. Wang, K. Takahashi, K. H. Lee, and G. Z. Cao, *Adv. Funct. Mater.*, 2006, **16**, 1133–1144.
7. J. M. Cocciantelli, M. Ménétrier, C. Delmas, J. P. Doumerc, M. Pouchard, M. Broussely, and J. Labat, *Solid State Ionics*, 1995, **78**, 143–150.
8. C. Delmas, H. Cognacauradou, J. Cocciantelli, M. Ménétrier, and J. Doumerc, *Solid State Ionics*, 1994, **69**, 257–264.
9. D. Murphy and P. Christian, *Inorg. Chem.*, 1979, **18**, 2800–2803.
10. P. Y. Zavalij and M. S. Whittingham, *Acta Cryst. B*, 1999, **55**, 627–663.
11. Y. Liu, M. Clark, Q. Zhang, D. Yu, D. Liu, J. Liu, and G. Cao, *Adv. Energy Mater.*, 2011, **1**, 194–202.
12. C. O'Dwyer and V. Lavayen, *Adv. Funct. Mater.*, 2009, **19**, 1736–1745.
13. C. Leger, S. Bach, P. Soudan, and J.-P. Pereira-Ramos, *J. Electrochem. Soc.*, 2005, **152**, A236.
14. F. Coustier, *J. Electrochem. Soc.*, 1999, **146**, 1355.
15. A. Marschilok, S. Davis, and R. Leising, *Coord. Chem. Rev.*, 2001, **221**, 283–310.
16. Y.-S. Hu, X. Liu, J.-O. Müller, R. Schlögl, J. Maier, and D. S. Su, *Angew. Chem. Int. Ed. Engl.*, 2009, **48**, 210–4.
17. M. Sathiy, a S. Prakash, K. Ramesha, J. M. Tarascon, and a K. Shukla, *J. Am. Chem. Soc.*, 2011, **133**, 16291–9.
18. G. Du, K. H. Seng, Z. Guo, J. Liu, W. Li, D. Jia, C. Cook, Z. Liu, and H. Liu, *RSC Adv.*, 2011, **1**, 690.
19. G. C. Bond and K. Brackman, *Farad. Discuss.*, 1981, **72**, 235.
20. M. G. Minett and J. R. Owen, *J. Power Sources*, 1990, **32**, 81–97.
21. K. Lee and G. Cao, *J. Phys. Chem. B*, 2005, **109**, 11880–5.
22. M. B. Sahana, C. Sudakar, C. Thapa, V. M. Naik, G. W. Auner, R. Naik, and K. R. Padmanabhan, *Thin Solid Films*, 2009, **517**, 6642–6651.
23. F. Bellenger, C. Chemarin, D. Deroo, S. Maximovitch, a. Surca Vuk, and B. Orel, *Electrochim. Acta*, 2001, **46**, 2263–2268.
24. K. Takahashi, Y. Wang, K. Lee, and G. Cao, *Appl. Phys. A*, 2005, **82**, 27–31.
25. A. Davies, R. Hobson, and M. Hudson, *J. Mater. Chem.*, 1996, **6**, 49–56.
26. N. Özer, S. Sabuncu, and J. Cronin, *Thin Solid Films*, 1999, **338**, 1–6.
27. J. Livage, *Chem. Mater.*, 1991, **3**, 578–593.
28. C. J. Patrissi, *J. Electrochem. Soc.*, 1999, **146**, 3176.
29. L. Fu, H. Liu, C. Li, Y. Wu, E. Rahm, R. Holze, and H. Wu, *Prog. Mater. Sci.*, 2005, **50**, 881–928.
30. T. Zhai, H. Liu, H. Li, X. Fang, M. Liao, L. Li, H. Zhou, Y. Koide, Y. Bando, and D. Golberg, *Adv. Mat.*, 2010, **22**, 2547–52.
31. B. Li, Y. Xu, G. Rong, M. Jing, and Y. Xie, *Nanotechnology*, 2006, **17**, 2560–6.
32. S.-L. Chou, J.-Z. Wang, J.-Z. Sun, D. Wexler, M. Forsyth, H.-K. Liu, D. R. MacFarlane, and S.-X. Dou, *Chem. Mater.*, 2008, **20**, 7044–7051.
33. N. Pinna, M. Willinger, K. Weiss, J. Urban, and R. Schlögl, *Nano Lett.*, 2003.
34. E. a. Ponzio, T. M. Benedetti, and R. M. Torresi, *Electrochim. Acta*, 2007, **52**, 4419–4427.
35. P. Ragupathy, S. Shivakumara, H. N. Vasan, and N. Munichandraiah, *J. Phys. Chem. C*, 2008, **112**, 16700–16707.
36. L. Mai, L. Xu, C. Han, X. Xu, Y. Luo, S. Zhao, and Y. Zhao, *Nano Lett.*, 2010, **10**, 4750–5.
37. Y. L. Cheah, N. Gupta, S. S. Pramana, V. Aravindan, G. Wee, and M. Srinivasan, *J. Power Sources*, 2011, **196**, 6465–6472.
38. H.-G. Wang, D.-L. Ma, Y. Huang, and X.-B. Zhang, *Chem. Eur. J.*, 2012, **18**, 8987–93.
39. C. Ban, N. a. Chernova, and M. S. Whittingham, *Electrochem. Commun.*, 2009, **11**, 522–525.
40. D. Yu, C. Chen, S. Xie, Y. Liu, K. Park, X. Zhou, Q. Zhang, J. Li, and G. Cao, *Energy Environ. Sci.*, 2011, **4**, 858.
41. K. Takahashi, S. Limmer, Y. Wang, and G. Cao, *J. Phys. Chem. B*, 2004, **108**, 9795–9800.
42. H. Yan, S. Sokolov, J. C. Lytle, A. Stein, F. Zhang, and W. H. Smyrl, *J. Electrochem. Soc.*, 2003, **150**, A1102.
43. P. Liu, S. H. Lee, C. E. Tracy, Y. Yan, and J. A. Turner, *Adv. Mat.*, 2002, **14**, 27.
44. A.-M. Cao, J.-S. Hu, H.-P. Liang, and L.-J. Wan, *Angew. Chem. Int. Ed. Engl.*, 2005, **44**, 4391–5.

-
45. Y. Wang, K. Takahashi, H. Shang, and G. Cao, *J. Phys. Chem. B*, 2005, **109**, 3085–3088.
46. X. Zhang, K. Wang, X. Wei, and J. Chen, *Chem. Mater.*, 2011, 5290–5292.
47. a.-H. Lu and F. Schüth, *Adv. Mat.*, 2006, **18**, 1793–1805.
48. H. Yang and D. Zhao, *J. Mater. Chem.*, 2005, **15**, 1217–1231.
49. Z. Li, M. Jaroniec, P. Papakonstantinou, J. M. Tobin, U. Vohrer, S. Kumar, G. Attard, and J. D. Holmes, *Chem. Mater.*, 2007, **19**, 3349–3354.
50. D. M. Burke, J. P. O’Byrne, P. G. Fleming, D. Borah, M. a. Morris, and J. D. Holmes, *Desalination*, 2011, **280**, 87–94.
51. B. C. Satishkumar, a. Govindaraj, M. Nath, and C. N. R. Rao, *J. Mater. Chem.*, 2000, **10**, 2115–2119.
52. P. Ajayan, O. Stephan, P. Redlich, and C. Colliex, *Nature*, 1995.
53. K. Everaert and J. Baeyens, *J. Hazard. Mater.*, 2004.
54. D. Su, M. Wieske, E. Beckmann, and A. Blume, *Catal. Lett.*, 2001, **75**, 81–86.
55. C. O’Dwyer, V. Lavayen, D. Fuenzalida, H. Lozano, M. a Santa Ana, E. Benavente, G. González, and C. M. Sotomayor Torres, *Small*, 2008, **4**, 990–1000.
56. G. Gannon, C. O’Dwyer, J. a Larsson, and D. Thompson, *J. Phys. Chem. B*, 2011, **115**, 14518–25.
57. X. Jiang and X. Chen, *J. Cryst. Growth*, 2004, **270**, 547–552.
58. A. Šurca, S. Benčič, B. Orel, and B. Pihlar, *Electrochim. Acta*, 1999, **44**, 3075–3084.
59. D. Murphy and P. Christian, *Inorg. Chem.*, 1979, **18**, 2800–2803.
60. A. Pan, J.-G. Zhang, Z. Nie, G. Cao, B. W. Arey, G. Li, S. Liang, and J. Liu, *J. Mater. Chem.*, 2010, **20**, 9193.
61. L. Kavan and M. Grätzel, *J. Am. Chem. Soc.*, 1996, **650**, 6716–6723.
62. G. N. Kryukova, D. O. Klenov, and G. A. Zenkovets, *React. Kinet. Catal. Lett.*, 1997, **60**, 179–187.
63. A. Vejux and P. Courtine, *J. Solid State Chem.*, 1978, **23**, 93–103.
64. D. Le, S. Passerini, and A. Tipton, *J. Electrochem. Soc.*, 1995, **142**, 1994–1995.

35